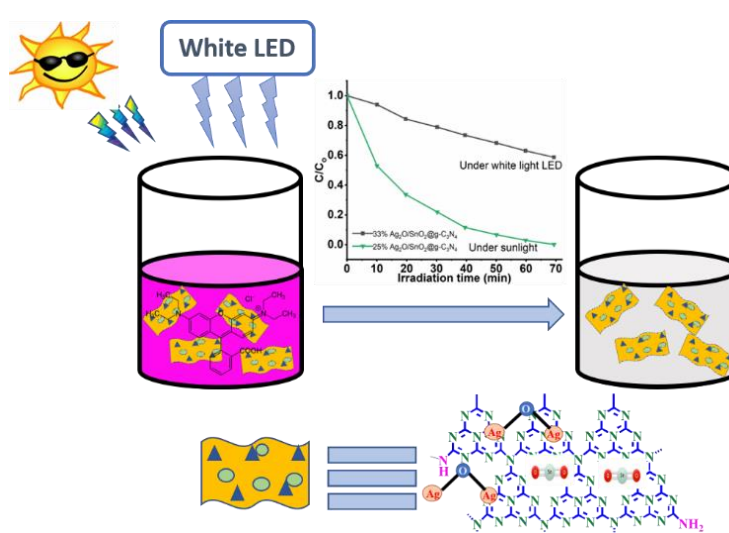# Chapter 6

Comparative Study of Enhanced Photodegradation of Azo Dye by Ternary Nanocomposite Ag_2O/SnO_2@g-C_3N_4 under Natural and Artificial Light Sources

In this chapter, the Photochemical dye degradation performance of graphitic carbon nitride - metal oxide based ternary nanocomposites has been discussed. We studied comparative photodegradation of common synthetic dye Rhodamine B used in the textile industry and as an illegal additive in food under two different light sources, natural sunlight and artificial white light-emitting diode (LED) with catalytic assistance of as-prepared Ternary nanocomposites: Ag_2O/SnO_2@g-C_3N_4.

6.1 Introduction

A clean environment and green energy are the most demanding in the present time. Such demand has led the scientific communities to an exploration of those materials that can reduce the stress of the environment and can also provide alternative energy solutions. [218,219] Visible light-based semiconductor photocatalyst such as TiO_2 had proven to be a good option for water splitting ability by Fujishima and Honda. [220] But, it has its own limitations owing to the fast recombination of electron-hole pairs and using only a very short range of incoming solar radiation. [221,222] ZnO also has a larger bandgap, showing absorbance in the UV region only. [223,224] Some other metal sulfides and mixed metal oxides like ZnS, CdS, $SrTiO_3$ have also been studied for photocatalytic application, however, these all have limited practical application due to fast recombination of the as-separated charge carriers under the influence of incident photo-exposure. [225-227] Certain modifications such as heterostructure formation with another metal oxides or with a conjugated polymer of suitable band gap have proved as a strategic approach to delay the recombination of photogenerated charge carriers. [228,229] The heterostructure of semiconductors is based on band alignment creating the heterojunction, which is widely applied in opto-electronics. The heterojunction made by two semiconductors is categorized into three categories based on band positions- Straddling gap (Type I), Staggered gap (Type II) and Broken gap (Type III). [27] The band alignment of the semiconductors promotes enhanced separation of charge carriers at the interface and their further utilization for catalytic purposes.

Noble metal-based metal oxide semiconductors such as Ag_2O show stronger absorption in the visible range due to their localized surface plasmon resonance (SPR).

Ag_2O has a narrow bandgap of 1.3 eV which makes it a suitable candidate for solar energy absorption and photochemically stable nature as well. Its heterostructure with another semiconductor metal oxides chosen on the alignment of band-offsets can significantly delay the recombination of charge carriers. Ag_2O nanoparticles (NPs) anchored on some suitable catalyst support viz. 2D material yields better photocatalytic results synergistically. [230-232]

SnO_2 is an n-type semiconductor widely used for application in energy storage, photocatalysis, gas-sensing, solar cells and Li-ion battery anode. SnO_2 is also thermally stable to high temperatures. The bandgap position of SnO_2 makes it a good choice to imply it in heterostructures with another metal oxide and $g-C_3N_4$ in order to drive the targeted photocatalytic process. [233,234]

On the other hand, two-dimensional graphitic carbon nitride (2D $g-C_3N_4$) has drawn wide research interest owing to being a metal-free catalyst, easy to synthesize, stable to a range of acid-alkaline solution and its non-toxicity. In over a decade, research based on 2D $g-C_3N_4$ has been explored for its numerous photocatalytic properties. It has been observed that $g-C_3N_4$ has a bandgap value of 2.7 eV and its absorption edge lies at 440 nm, which makes it a good absorber especially in the visible range. [31,89,235,236] However, the application of pristine $g-C_3N_4$ is limited due to faster recombination of charge carriers, low surface area, poor charge mobility and low quantum efficiency. Therefore, blending this photocatalytic material with suitable polymer or impregnation with metal oxide/carbonates/halides/phosphates and other noble metals nanoparticles of comparable band gap can greatly improve its photodegradation efficiency. [84, 237-242] Usually, the selection of co-catalyst is based on the principle of bandgap alignment and adhesion with $g-C_3N_4$. The formed

heterostructures are usually binary and ternary nanocomposites giving an enhanced performance to its individual components.

Rhodamine B is a widely used dye for industrial purposes and its discharge from wastewater poses a serious environmental and biological threat. Biochemical and physicochemical methods are the conventional ways for removal of this azo dye and proved to be less effective. Semiconductor-based heterogeneous photocatalysis has come out to be an effective way for organic dye degradation. [243]

In view of the above, we took the advantage of the knowledge of bandgap engineering and synthesized a ternary nanocomposite that shows enhanced dye degradation efficiency both under natural sunlight and artificial white light LED. The ternary nanocomposite was prepared by fabricating an optimum ratio of two different semiconductor metal oxides (Ag_2O and SnO_2 NPs) over the g-C_3N_4 structure in a two-step synthesis approach. Thereafter, with the help of as-synthesized ternary nanocomposite, an enhanced capability of rhodamine B dye degradation was achieved compared among individual components and binary counterparts, credit to delayed recombination of photogenerated charge carriers. The SnO_2 and Ag_2O NPs have Type-I heterojunctions viz. straddling gap, while g-C_3N_4 and SnO_2 form Type-II viz. staggered gap, resulting in greater separation of photogenerated charge carriers e- and h^+. The 25% metal oxides loaded g-C_3N_4 nanocomposite excels among others when catalyst-dye dispersion was irradiated with sunlight, while 33% metal oxides loaded g-C_3N_4 heterostructure excels the Rh B degradation performance under irradiation of white light LED. The plausible mechanism has also been elaborated for its enhanced catalytic properties.

6.2 Experimental

6.2.1 Materials

Melamine (Extra Pure) and Ethylene glycol (for analysis) were purchased from Loba Chemie, India and Merck, India respectively. $AgNO_3$ (99.99%; trace metal basis) was purchased from Sigma Aldrich. $SnCl_4.5H_2O$ (98.0%) and Urea (for molecular biology) were procured from SRL, India. All other chemicals used were of analytical grade and used as received.

6.2.2 Synthesis of Pure g-C$_3$N$_4$

The bulk g-C$_3$N$_4$ was prepared by heating 5 g of melamine in an alumina crucible covered with lid into a muffle furnace at the temperature of 550°C in the close air atmosphere for 4 h with the ramp rate of 3°C/min. The as-obtained pale yellow hard stuff was grounded into a fine powder using agate mortar-pestle and preserved in a vacuum desiccator for further characterizations.

6.2.3 Synthesis of Binary Ag$_2$O@g-C$_3$N$_4$ and SnO$_2$@g-C$_3$N$_4$ Nanocomposites

We prepared binary g-C$_3$N$_4$ - metal oxides heterostructures as follows: a fixed weight of 0.4 gram of finely grounded g-C$_3$N$_4$ powder was dispersed in 10 ml of 0.5M NaOH solution by constant sonication. Thereafter, 0.1 gram of $AgNO_3$ dissolved in an aqueous solution was added dropwise into the above alkaline dispersion under constant stirring. A blackish-brown precipitate was observed immediately which was filtered using Whatman filter paper and washed several times using the double-distilled water till the pH of filtrate becomes 7. As-synthesized blackish-brown filtrate was vacuum dried at 60°C and termed as 25% Ag$_2$O@g-C$_3$N$_4$ binary nanocomposites. In a similar way, 33

% $Ag_2O@g-C_3N_4$ was prepared with mass loading of ~0.1 g of silver oxide over the 0.3 g of $g-C_3N_4$ material.

For the synthesis of $SnO_2@g-C_3N_4$ heterostructure, 0.4 gram of $g-C_3N_4$ material was dispersed into 20 ml of ethylene glycol under stirring for 3 h. 0.1 gram of $SnCl_4.5H_2O$ was added into the dispersion followed by 0.1 g of urea (dissolved in water) as a reducing agent under rapid stirring condition. This reaction mixture was transferred into a 25 ml capacity Teflon-lined steel autoclave and heated at 180°C for 16 h in the oven. Herein, urea acts as a precipitating agent by hydrolyzing itself into ammonium hydroxide and changes $SnCl_4$ to $Sn(OH)_4$, that further converted to SnO_2 at elevated temperature. The as-obtained binary nanocomposite was washed several times with de-ionized water in order to remove excess unreacted precursors and vacuum dried at 80°C for 24 h. It was designated as 25% $SnO_2@g-C_3N_4$. In a similar fashion, 33% $SnO_2@g-C_3N_4$ was prepared using 0.1 g of Sn salt and 0.3 g of $g-C_3N_4$ material.

6.2.4 Synthesis of $Ag_2O/SnO_2@g-C_3N_4$ Nanocomposite

Ternary nanocomposite ($Ag_2O/SnO_2@g-C_3N_4$) was prepared in a two-step rational synthesis process as a combination of the above two, first precipitation method is used to synthesize Ag_2O nanoparticles over the surface of $g-C_3N_4$ and then the hydrothermal synthesis method is adopted to amalgamate the SnO_2 nanoparticles over the binary nanocomposite $Ag_2O@g-C_3N_4$. Figure 6.1 shows a schematic representation of the adopted synthesis protocol for ternary nanocomposite.
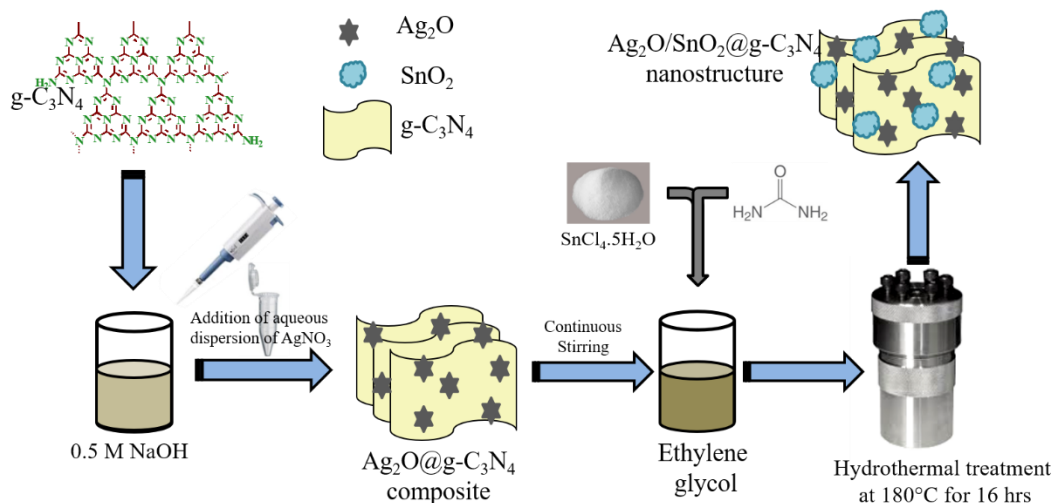
Fig. 6.1 Synthesis protocol of ternary nanocomposite (Ag$_2$O/SnO$_2$@g-C$_3$N$_4$).

First, 25 % Ag$_2$O@g-C$_3$N$_4$ was prepared by the protocol described, thereafter 0.4 gram of it was dispersed into the ethylene glycol and 0.1 gram of SnCl$_4$.5H$_2$O was added into the dispersion followed by Urea as a reducing agent. Hydrothermal treatment of mixture for a prolonged time (16 h) at 180 °C results into Ag$_2$O/SnO$_2$@g-C$_3$N$_4$ composite and enhancement of its surface area under high pressure and temperature. We adopted the above synthesis sequence in order to avoid any alteration in the surface nature of as-prepared SnO$_2$ by pH of the solution environment. This composite is termed 25 % Ag$_2$O/SnO$_2$@g-C$_3$N$_4$-11. Herein, prefix 25% represents the total contents of Ag$_2$O and SnO$_2$ in g-C$_3$N$_4$ matrix, while suffix '11' represents the mass ratio of 1:1 from its precursor side during the synthesis process.

In a similar fashion, 33% Ag$_2$O/SnO$_2$@g-C$_3$N$_4$-11 with 1:1 ratio for silver and tin oxide nanoparticles was prepared. We also prepared the ternary heterostructure by varying the Ag$_2$O:SnO$_2$ ratio in 1:4 and 4:1 in 25% Ag$_2$O/SnO$_2$@g-C$_3$N$_4$ and designated them as 25 % Ag$_2$O/SnO$_2$@g-C$_3$N$_4$-14 and 25 % Ag$_2$O/SnO$_2$@g-C$_3$N$_4$-41

respectively. Similarly, 33% $Ag_2O/SnO_2@g$-C_3N_4-12 and 33 % $Ag_2O/SnO_2@g$-C_3N_4-21 were prepared with 1:2 and 2:1 ratio of Ag_2O:SnO_2. This change of variation of metal oxides is designed to investigate the AgO_2/SnO_2 as the control sample and synergism between the two for dye degradation. In addition, pure Ag_2O and SnO_2 nanoparticles were also synthesized by precipitation and hydrothermal methods respectively.

In the present case of study, 33% $Ag_2O/SnO_2@g$-C_3N_4-11 nanocomposite is chosen and compared for structural and morphological analysis with individual and binary counterparts while other fractions of nanocomposite are included for the comparison of dye degradation efficiencies.

6.2.5 Characterization Tools

UV-DRS spectra were obtained from Shimadzu UV-VIS (UV-2600i) spectrophotometer, while photoluminescence spectra (PL) were recovered from the F-4600 FL spectrophotometer. XRD data was recovered from Rigaku mini flex 600 X-ray diffractometer having Ni-filtered Cu $K_{\alpha 1}$ radiation (λ= 1.54056 Å) at a scan rate of 3 °/min. FT-IR vibration spectrum was recorded from the Thermo Scientific NICOLET iS5 instrument. Transmission electron microscope (TEM) images were captured from FEI, TECNAI G^2 20 TWIN instrument at an accelerating voltage of 200 kV. Field emission scanning electron microscope (FESEM) images were obtained from FEI NOVA NANO SEM 450 instrument. Both for FESEM and TEM, the sample preparation was carried out by casting a small amount of dispersed materials in THF solvent. X-ray photoelectron spectra (XPS) were obtained son Thermo Fischer Scientific ESCALAB Xi+. N_2 adsorption-desorption isotherms were obtained from the

Belsorp Max II instrument at liquid N_2 temp. of 77 K after pretreatment of 6 hrs in a vacuum.

6.3 Results and Discussion

6.3.1 Structural Analysis

After the synthesis of all sets of materials, they are characterized for their structural implications by various characterization tools. Figure 6.2 (a) represents XRD spectra of g-C_3N_4, pure Ag_2O NPs, Pure SnO_2 NPs, 33% SnO_2@g-C_3N_4, 33% Ag_2O@g-C_3N_4 and 33% Ag_2O/SnO_2@g-C_3N_4-11 nanocomposites along with diffraction planes. The diffraction peak of g-C_3N_4 at $2\theta = 27.6°$ is characteristic of its hexagonal phase (JCPDS No. 87-1526) corresponding to the (002) crystallographic plane. This type of evidence appears due to the stacking of 2D layers of g-C_3N_4 at the inter planer distance of 0.326 nm as obtained from Bragg's law. This diffraction peak appears in all g-C_3N_4 containing composites as a major peak confirming the identity of g-C_3N_4 does not lose even in the applied synthesis conditions. In the Pure Ag_2O NPs XRD pattern, three major diffraction peaks spotted at $2\theta = 33.0°$, $38.4°$ and $55.3°$ were assigned to the crystallographic plane (111), (200) and (220) respectively. It confirms the cubic phase (JCPDS card no. 41-1104) of the synthesized Ag_2O NPs. The diffraction pattern of binary 33% Ag_2O@g-C_3N_4 nanocomposite has characteristics peaks of both the constituents, the relative peak intensities of Ag_2O NPs is less due to the low amount of nanoparticles decorated over the g-C_3N_4 structure. Pure SnO_2 exhibits major diffraction peaks at $2\theta = 27.5°$, $34.6°$, $52.8°$ and $66.0°$ corresponding to crystallographic planes (110), (101), (211) and (301) respectively and that is a characteristic of its tetragonal phase (JCPDS card no. 41-1445). In the case of 33% SnO_2@g-C_3N_4 nanocomposite,

the major SnO_2 peak appears as a small hump with a shift to lower angle. This small shift appears due to the interaction of SnO_2 NPs with the g-C_3N_4 matrix, leading to enhancement in its d-spacing value compared to pure SnO_2 NPs. Ternary heterostructure 33%-Ag_2O/SnO_2@g-C_3N_4-11 exhibits major peaks of both individuals Ag_2O and SnO_2 NPs along with the peak of g-C_3N_4. (111) peak of Ag_2O NPs and (101) peak of SnO_2 NPs appears to be merged and seen as a small hump at $2\theta = 33.9°$ in the XRD pattern. The (200) diffraction plane of Ag_2O NPs and (211) plane of SnO_2 NPs were also identified in the ternary nanocomposite.
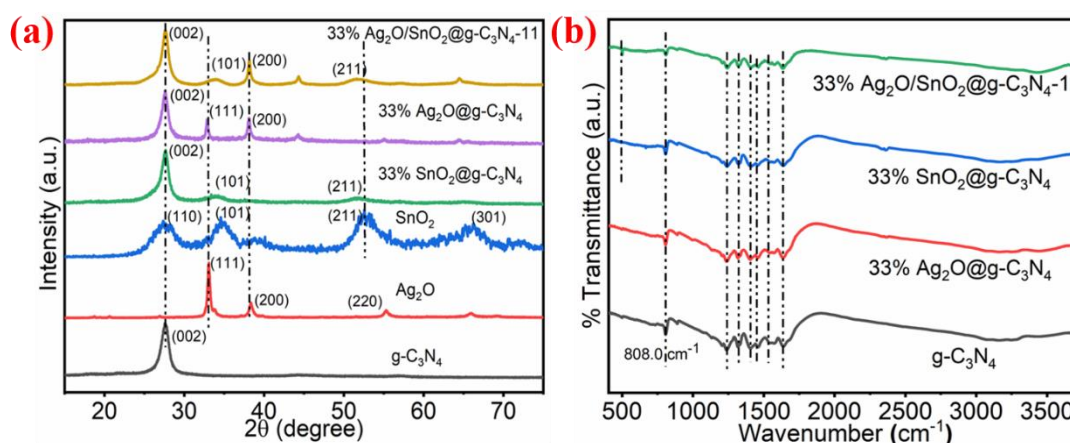
Fig. 6.2 (a) XRD pattern of g-C_3N_4 and 33% metal oxide loaded g-C_3N_4 composites and (b) vibrational spectra of bulk g-C_3N_4 and other counterparts.

Vibrational spectra of metal oxide nanoparticles (Ag_2O and SnO_2), g-C_3N_4 and as-prepared nanocomposites were recorded on FTIR instrument in order to verify the identity of individuals. As visible in Figure 6.2 (b), g-C_3N_4 shows its characteristic vibration peaks of triazine units at 808.0 cm^{-1} which is distinct in all g-C_3N_4 containing composites. Fingerprint region is observed from 1235 to 1642 cm^{-1} region, while at

around 3220 cm^{-1} stretching mode of N-H of g-C$_3$N$_4$ is obtained. SnO$_2$ NPs show stretching bands of Sn-O at 567.8 and 654.3 cm^{-1} respectively (Appendix A Fig.A.9-a), these peaks are also visible in SnO$_2$ NPs containing nanocomposites. [234,84] Ag-O vibrational peaks were observed in nano Ag$_2$O at around 594 cm^{-1} and 1393.8 cm^{-1}, while the peak at 1651 cm^{-1} and broad hump at 3400 cm^{-1} were attributed to bending and stretching mode of residual H$_2$O respectively (Appendix A Fig.A.9-b). [232] Binary 33% Ag$_2$O@g-C$_3$N$_4$ nanocomposite exhibits all characteristics vibration peaks of Ag$_2$O NPs along with peaks of g-C$_3$N$_4$, while 33% SnO$_2$@g-C$_3$N$_4$ also retains its identity by exhibiting corresponding peaks of constituents SnO$_2$ NPs and g-C$_3$N$_4$. Similarly, the ternary nanocomposite Ag$_2$O/SnO$_2$@g-C$_3$N$_4$ has the vibration peaks of both metal oxides merged with featured peaks of g-C$_3$N$_4$.

6.3.2 Elemental Analysis of Ternary Composites

The bonding states of possible elements in the ternary nanocomposite were studied by X-ray photoelectron spectroscopy (XPS). Firstly, the full scan survey spectrum of 25% Ag$_2$O/SnO$_2$@g-C$_3$N$_4$-11 is recorded as shown in Figure 6.3 (A) along with high-resolution individual spectra of constituting elements C1s, N1s, O1s, Ag3d and Sn3d. All the peak positions in high-resolution spectra show some shift (in decimals) of binding energy compared to parental materials owing to hydrothermal treatment and coupling with metal oxides. The high-resolution C1s peak has deconvoluted into four component peaks positioned at 284.4 eV, 285.4 eV, 286.4 and 289.0 eV assigned to sp^2 C—C bond (and adventitious carbon), a combination of C—N group, sp^2
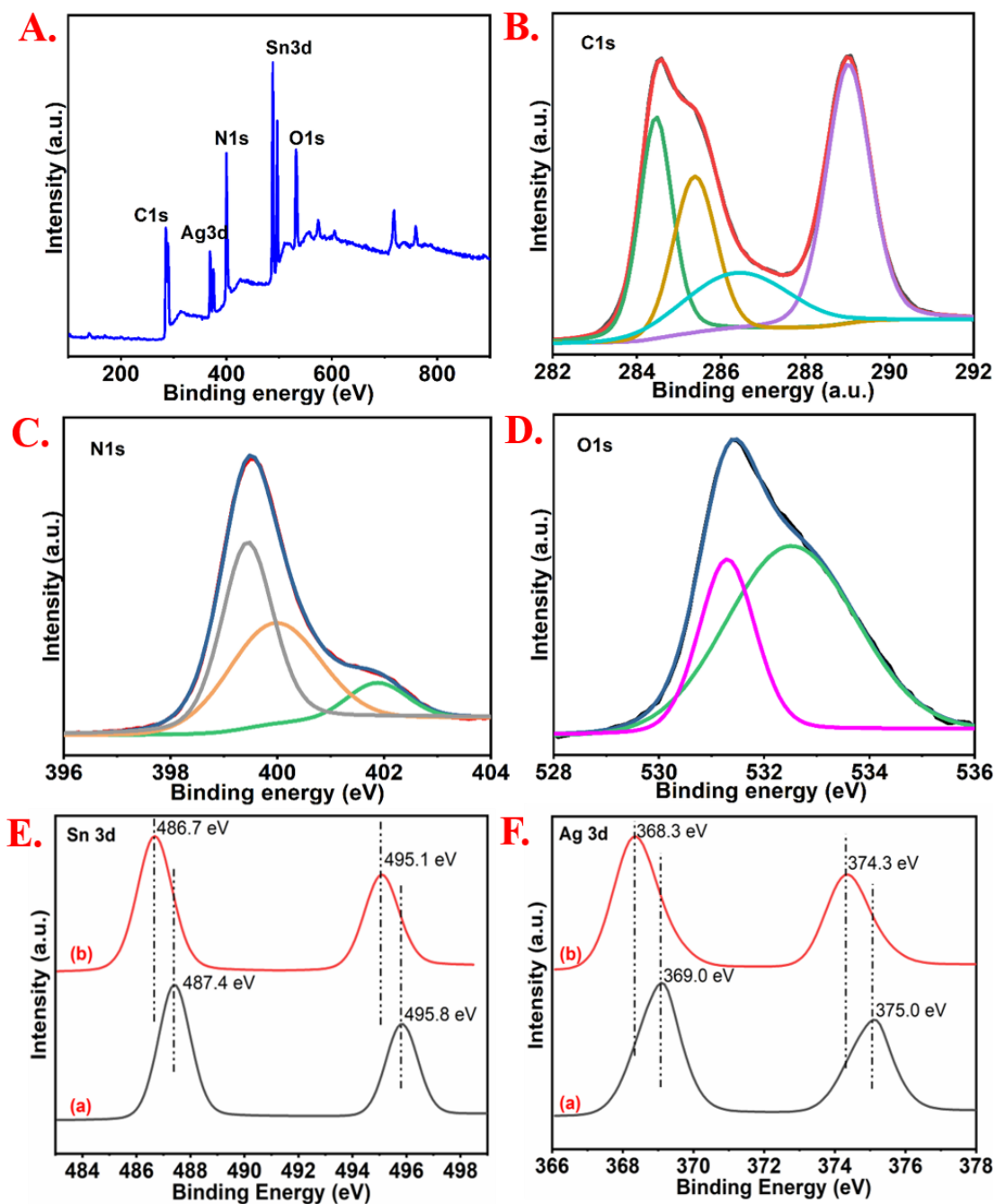
Fig. 6.3 XPS (A) survey analysis, (B) C1s, (C) N1s, (D) O1s for 25% Ag$_2$O/SnO$_2$@g-C$_3$N$_4$-11 and comparative analysis of (E) Sn3d and (F) Ag3d for (a) 25% Ag$_2$O/SnO$_2$@g-C$_3$N$_4$-11 (E-a/F-a) with pure SnO$_2$ (E-b) and Ag$_2$O (F-b) respectively.

Table 6.1 Binding states and peak positions of constituting elements of ternary nanocomposites.

Elements	Binding States	Peak Positions (eV)
C1s	C—C	284.4
	C—N	285.4
	N—C=N	286.4
	C—(N)$_3$	289.0
N1s	pyridinic N	399.4
	graphitic N	399.9
	—NH$_2$/=NH	401.9
O1s	Lattice O	531.3
	Surface —OH	532.5
Sn3d	Sn 3d$_{5/2}$	487.4
	Sn 3d$_{2/3}$	495.8
Ag3d		369.0
		375.0

carbon atom of N—C=N environment and C—(N)$_3$ groups of g-C$_3$N$_4$ respectively. The N1s peak consists of three deconvoluted heights at 399.4 eV, 399.9 eV and 401.9 eV corresponding to pyridinic N, graphitic N and —NH$_2$/=NH groups respectively. [232,92,157] The deconvoluted O1s peak were located at 531.3 and 532.5 eV designated to lattice and chemisorbed oxygen (surface —OH) of Ag$_2$O respectively. [232]

The high-resolution Sn3d ((a); black line) has peak positioned at 487.4 eV and 495.8 eV attributed to Sn 3d$_{5/2}$ and Sn 3d$_{2/3}$ respectively. A smaller shift (0.7 eV) to higher binding energy is clearly visible to pure SnO$_2$ ((b); red line), owing to interaction with 2D g-C$_3$N$_4$ as also confirmed in reported works of literature. [234] Ag3d ((a); black line) has two peaks positioned at 369.0 eV and 375.0 eV, again a small shift (0.7

eV) to higher binding energy compared to pure Ag_2O ((b); red line), confirming interaction of Ag_2O into the composite material. [232] The binding states and peak positions of all constituting elements of ternary nanocomposite are also tabulated in Table 6.1. Hence, XPS spectral study confirms the presence of assumed elements with a small shift in binding energy further verifies the surface interaction between $g-C_3N_4$ and metal oxide nanoparticles.

6.3.3 Optical Analysis

Since our target was to synthesize materials having a broad absorption range based on the band alignment engineering and capable of degrading the chosen dye. That is why, optical band gap calculation and its comparison are necessary. Absorption properties of as-synthesized nanocomposites and semiconductor nanoparticles were studied by UV-vis diffuse reflectance spectra (DRS) as shown in Figure 6.4(A) and Appendix A Figure A.10 respectively. Bulk $g-C_3N_4$ has an absorption edge around wavelength = 470 nm corresponding to the bandgap of 2.65 eV. DRS spectrum of $Ag_2O/g-C_3N_4$ covers a broader range up to wavelength =800 nm, while $SnO_2@g-C_3N_4$ has absorption spectra almost similar to that of the $g-C_3N_4$ spectrum. The absorption range effect of ternary composite $Ag_2O/SnO_2@g-C_3N_4$ in presence of two nano metal oxides extends up to wavelength= 800 nm. Such broad coverage of wavelength both in UV and visible region will help greater harvest of photo energy in the case of the ternary photocatalyst. The optical bandgap of the semiconductors was calculated from the Tauc method, further developed by Davis and Mott using UV-vis DRS absorption spectra as shown in Figure 6.4(B). [244, 245]
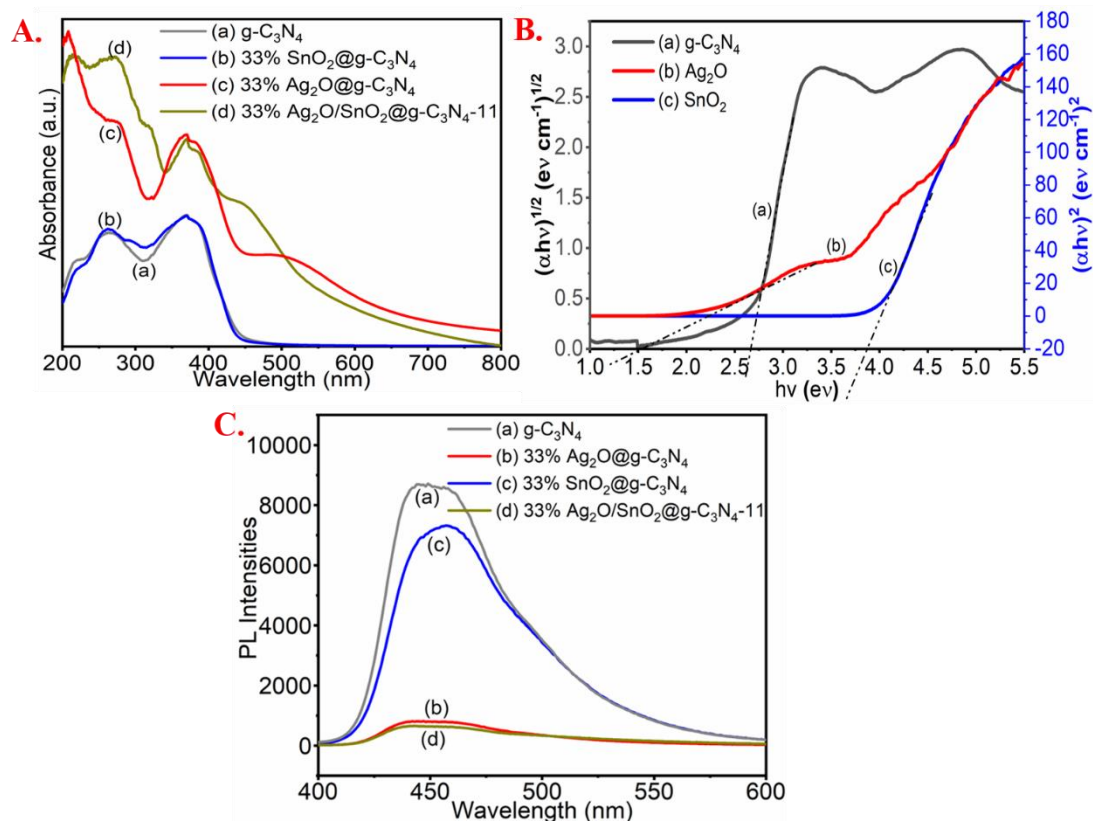
Fig. 6.4(A). UV-vis DRS spectra of (a) g-C_3N_4, (b) 33% SnO_2@g-C_3N_4, (c) 33% Ag_2O@g-C_3N_4 and (d) 33% Ag_2O/SnO_2@g-C_3N_4; 6.4(B). Plot of $(\alpha h\nu)^{1/2}$ *vs* hν for band gap energy of (a) g-C_3N_4 and $(\alpha h\nu)^2$ vs hν for bandgap energy of (b) Ag_2O and (c) SnO_2; and 6.4(C). Photoluminescence spectra (PL) of (a) g-C_3N_4, (b) 33% Ag_2O@g-C_3N_4, (c) 33% SnO_2@g-C_3N_4 and (d) 33% Ag_2O/SnO_2@g-C_3N_4 composites.

The bandgap was obtained using the following equation

$$\alpha h\nu = B(h\nu - E_g)^{n/2} \ldots\ldots\ldots\ldots\ldots\ldots\ldots\ldots.(Eq.\ 6.1)$$

Where α is absorption coefficient, *h* is Planck's constant, ν is frequency, B is a constant and E_g is bandgap energy. The value n depends on the kind of electron transition. For

g-C_3N_4 (indirect transition), Ag_2O and SnO_2 (direct transition in both), the value of n obtained is 4, 1 and 1 respectively. The bandgap values of g-C_3N_4, Ag_2O and SnO_2 were estimated to be 2.65, 1.5 and 3.82 eV respectively by extrapolating the tangent at the onset of absorption.

In order to get more insight into the generation and separation of photogenerated charge carriers (viz. e- and h+) in the as-prepared composite materials, steady-state photoluminescence (PL) measurement was performed at an excitation wavelength of 325 nm (*see* Fig. 6.4-C). It has been interpreted that, stronger PL intensity corresponds to fast recombination of charge carriers, while weaker PL intensity indicates slow recombination probability of free charge carriers. [92, 248-250] g-C_3N_4 has the highest PL intensity among other counterparts, confirming the fastest recombination of photogenerated e^- and h+ among others. The presence of optimum semiconductor metal oxides in both of the binary composite mitigates the faster recombination of e^--h^+ pairs. 33% $Ag_2O@g$-C_3N_4 composite has a significantly small PL emission intensity, hence a more delayed or slower recombination process. Ternary nanocomposite 33% $Ag_2O/SnO_2@g$-C_3N_4-11 with the lowest PL intensity signifies greater delay and larger separation of charge carriers from recombination once photogenerated. We also recorded transient photoluminescence spectra (time-resolved PL decay) to quantitatively investigate the carrier's lifetime as shown in Figure 6.5. The obtained average life time (τ_{avg}) for charge carriers into the base material g-C_3N_4 and 33% $Ag_2O/SnO_2@g$-C_3N_4-11 is 0.81 and 1.24 ns respectively. The obtained value is low to others earlier reported values for g-C_3N_4, [246-248] we believe this is due to the higher excitation wavelength of 405 nm (a criterion for the instrument), hence low energy excitation leads to weaker emission and shorter life time for charge carriers.

Comparatively, the ternary composite has a greater average life-time for separated charge carriers, credit to the optimum combination and suitable selection of cocatalyst and its band position in the heterojunction.
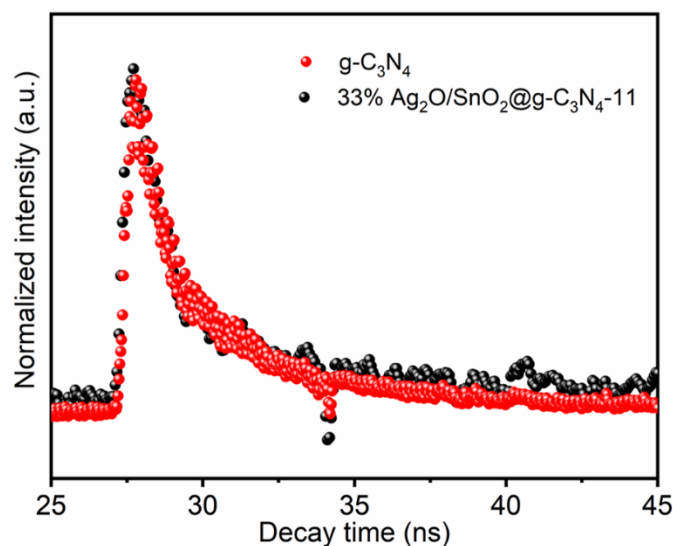

**Fig. 6.5** Time resolved PL decay spectra for the charge carrier in the g-C$_3$N$_4$ and 33% Ag$_2$O/SnO$_2$@g-C$_3$N$_4$-11.

6.3.4 Morphological Analysis

The morphological analysis of metal oxide-carbon nitride nanostructures was analyzed by TEM images. Figure 6.6 shows the TEM images of the as-prepared 33% Ag$_2$O@g-C$_3$N$_4$, 33% SnO$_2$@g-C$_3$N$_4$ and 33% Ag$_2$O/SnO$_2$@g-C$_3$N$_4$ nanocomposites at the same scale (50 nm) for the sake of comparison. The homogeneous distribution of metal oxide nanoparticles in the g-C$_3$N$_4$ matrix is easily distinguishable in either case of materials. From Figure 6.6(a), it is evident that Ag$_2$O nanoparticles of particle dimension 5.0 to 12.0 nm were uniformly anchored over g-C$_3$N$_4$ structure while, SnO$_2$ nanoparticles of relatively smaller size 2.5 to 5.0 nm were observed over g-C$_3$N$_4$ matrix in 33% SnO$_2$/g-

C_3N_4 binary nanocomposite (Fig. 6.6-b) as measured using Image J software. The smaller size of SnO_2 NPs to Ag_2O NPs might be attributed to the hydrothermal synthesis approach for SnO_2. Figure 6.6 (c) and (d) are TEM and HRTEM images of 33% $Ag_2O/SnO_2@g-C_3N_4$ respectively, both the metal oxides were identified over the g-C_3N_4 sheets by evaluating the d-spacing of the visible lattice fringes. The d-spacing measured for Ag_2O and SnO_2 nanoparticles were 0.263 and 0.320 nm respectively, which belongs to (111) and (110) planes, respectively. The reduction in the size of Ag_2O nanoparticles was also observed due to the prolonged hydrothermal treatment. Selected area electron diffraction (SAED) patterns of the ternary nanocomposite were indexed into relevant (hkl) plane of Ag_2O, SnO_2 and g-C_3N_4 in Figure 6.6 (e).
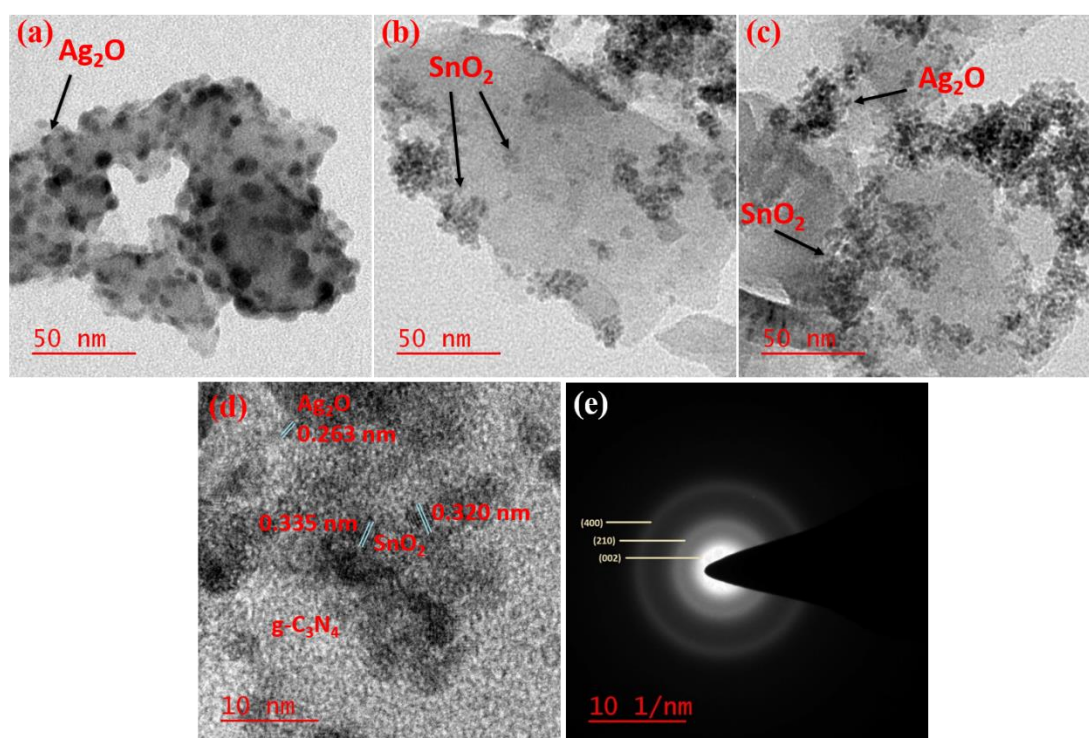
Fig. 6.6 TEM images of (a) 33% $Ag_2O@g-C_3N_4$, (b) 33% $SnO_2@g-C_3N_4$, (c) 33% $Ag_2O/SnO_2@g-C_3N_4$, (d) HRTEM image of 33% $Ag_2O/SnO_2@g-C_3N_4$, and corresponding (e) SAED pattern of 33% $Ag_2O/SnO_2@g-C_3N_4$.
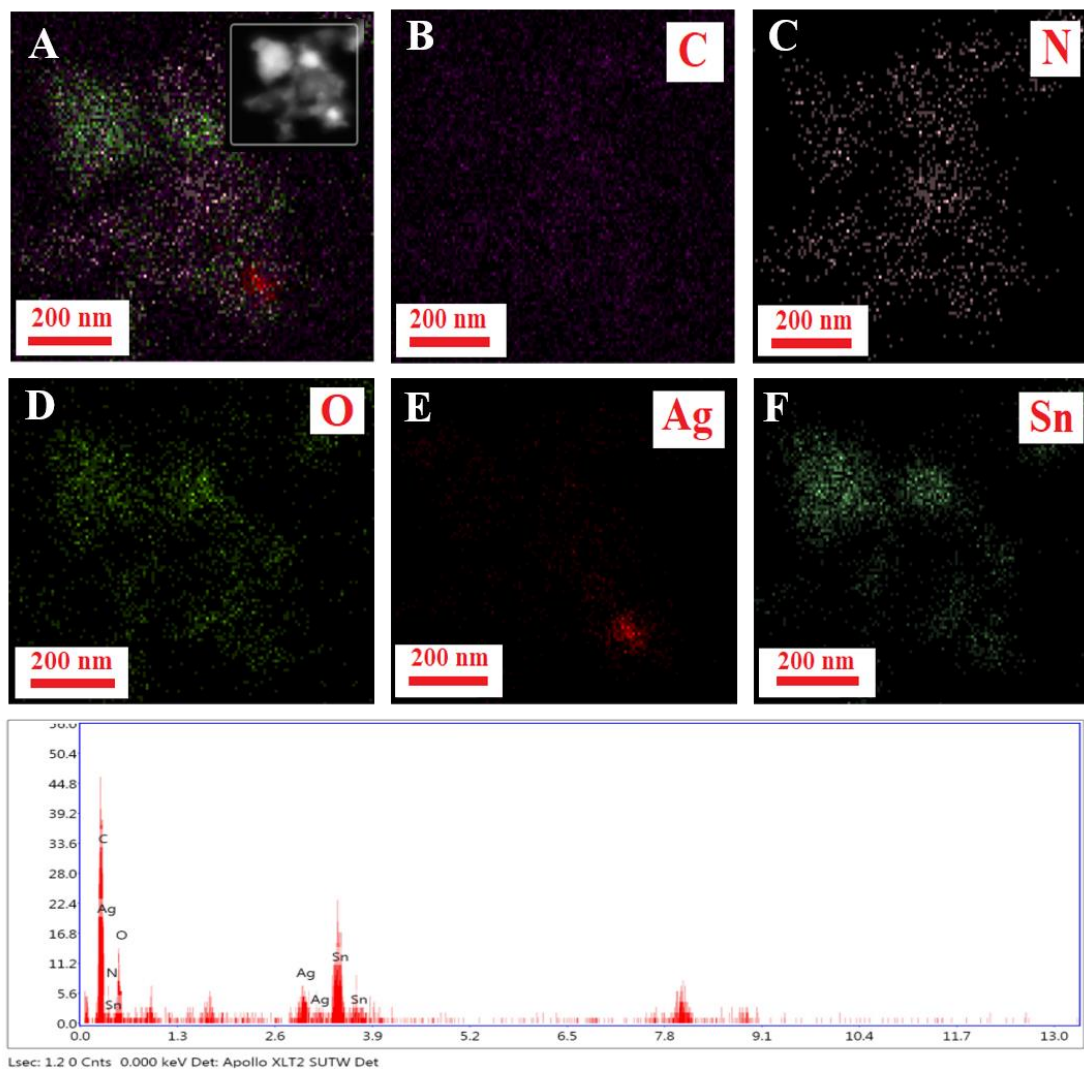
**Fig. 6.7** TEM elemental mapping of 33% $Ag_2O/SnO_2@g\text{-}C_3N_4$ and corresponding EDX spectrum.
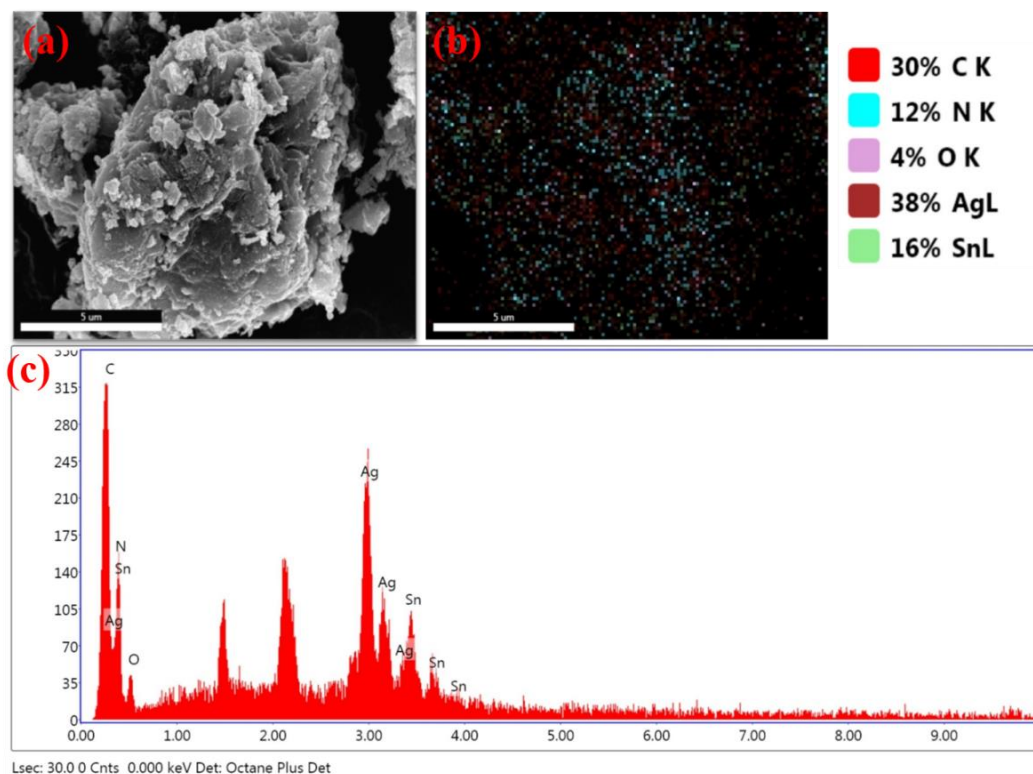
Fig. 6.8 FESEM image of 25% Ag$_2$O/SnO$_2$@g-C$_3$N$_4$ along with elemental mapping and EDX spectrum.

Irregular distribution of Ag$_2$O and SnO$_2$ nanoparticles were confirmed by elemental mapping by EDS on TEM and SEM micrographs (as shown in the inset of Fig. 6.7 and Fig. 6.8 respectively) which represents different colored spots corresponding to individual elements.

Since photocatalysis is a surface phenomenon where adsorbate (azo dye) lies over the adsorbent's surface (nanocomposite materials), the surface area of the as-prepared photocatalysts were measured from the N$_2$ adsorption-desorption isotherm on the basis of Brunauer–Emmett–Teller (BET) theory as shown in Figure 6.9 (A). g-C$_3$N$_4$

and 33% Ag_2O@g-C_3N_4 exhibit type II isotherms with a small hysteresis loop in the relative pressure range of 0.4 to 1.0, while 33% SnO_2@g-C_3N_4 and 33% Ag_2O/SnO_2@g-C_3N_4-11 had type IV isotherms with hysteresis loop of type H3. The single point BET specific surface area (a_s) of g-C_3N_4 was found to be 10.43 m^2/g, such a low surface area value is its characteristics feature as described earlier. The loading of Ag_2O NPs over the g-C_3N_4 led to further reduction into the specific surface area with a low value of 9.28 m^2/g for binary 33% Ag_2O@g-C_3N_4 composite. 33% SnO_2@g-C_3N_4 has a specific surface area value of 51.45 m^2/g, this high value was obtained due to the hydrothermal synthesis technique that causes weakening of van der Waals force between the layers of g-C_3N_4 and rupturing of sheet structure. Nanocomposite 33% Ag_2O/SnO_2@g-C_3N_4-11 has a surface area value of 41.58 m^2/g, again the presence of Ag_2O NPs led to reduction in surface area value as compared to 33% SnO_2@g-C_3N_4 composite. The pore volume distribution of these heterostructures is obtained from the Barrett-Joyner-Halenda (BJH) theory (Fig. 6.9 B) and the observed trend is similar to the surface area. Both measured values- specific surface area and average pore volume are tabulated in Table 6.2. It was inferred that ternary nanocomposite exhibits higher surface area with mesoporous features, hence tends to more adsorption of dye over its surface, resulting in the faster degradation process described in the later section.
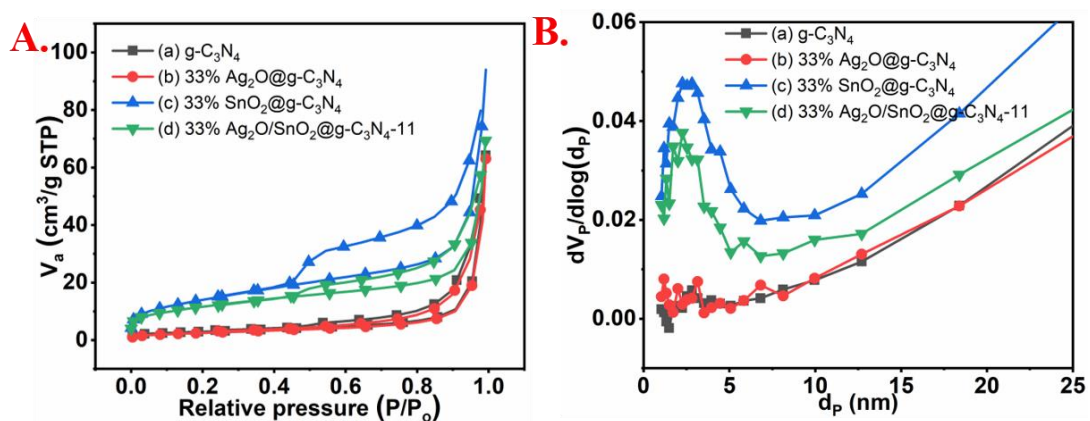
Fig. 6.9 N_2 adsorption-desorption isotherm of nanocomposites and corresponding pore volume distribution plot.

Table 6.2 Specific surface area and average pore volume of the nanocomposites and g-C_3N_4.

Photocatalysts	Specific Surface Area: a_s (m^2/g)	Average Pore Volume x 100 (cm^3/g)
g-C_3N_4	10.43	9.73
33% Ag$_2$O@g-C_3N_4	9.28	9.38
33% SnO$_2$@g-C_3N_4	51.45	14.61
33% Ag$_2$O/SnO$_2$@g-C_3N_4-11	41.58	10.15

6.3.5 Photocatalytic Degradation Study under Different Light Sources

All the photocatalytic study was performed by choosing a stock solution of 5 mg/L Rhodamine B dye and 50 mg of as-synthesized catalyst in all tests. Before exposing the catalytic dispersion to the desired light source, the dispersion was stirred for 30 min under dark to reach the equilibrium of dye adsorption at the catalyst surface. Catalytic dye degradation was performed in Borosil conical flask of 100 ml volume and mouth was covered using a glass slide to avoid change in concentration, if any, by evaporation. We choose two different light sources for irradiation of catalyst-dye dispersion, natural sunlight and artificial white light LED (Light Emitting Diode). Experiments under sunlight were performed simultaneously of all the samples same day and at the same time to minimize any error of variation in light intensity. Sunlight irradiation was performed mid-day in the month of January 2021 with average temp. recorded ~25ºC, while white light LED irradiation was performed using a 40-watt LED lamp (λ = 450-475 nm; lumens = 800 approx.) in a closed chamber at an average lab temperature of 20 ºC.

Figure 6.10 (A) shows the dye degradation performance of various catalysts under sunlight as a function of C/C_0 *vs*. irradiation time (C is dye conc. at t time, say 10, 20, 30 min and C_0 is dye conc. just before exposure to the light source i.e., 0 time). Pure g-C_3N_4 shows poor dye degradation ability compared to others, while all binary catalysts have comparable dye degradation performance owing to the coupling of metal oxide to the g-C_3N_4 surface. Ternary composites 25% Ag_2O/SnO_2@g-C_3N_4-11 excels with 99.98% dye degradation in 70 minutes as shown in Figure 6.10 (B).
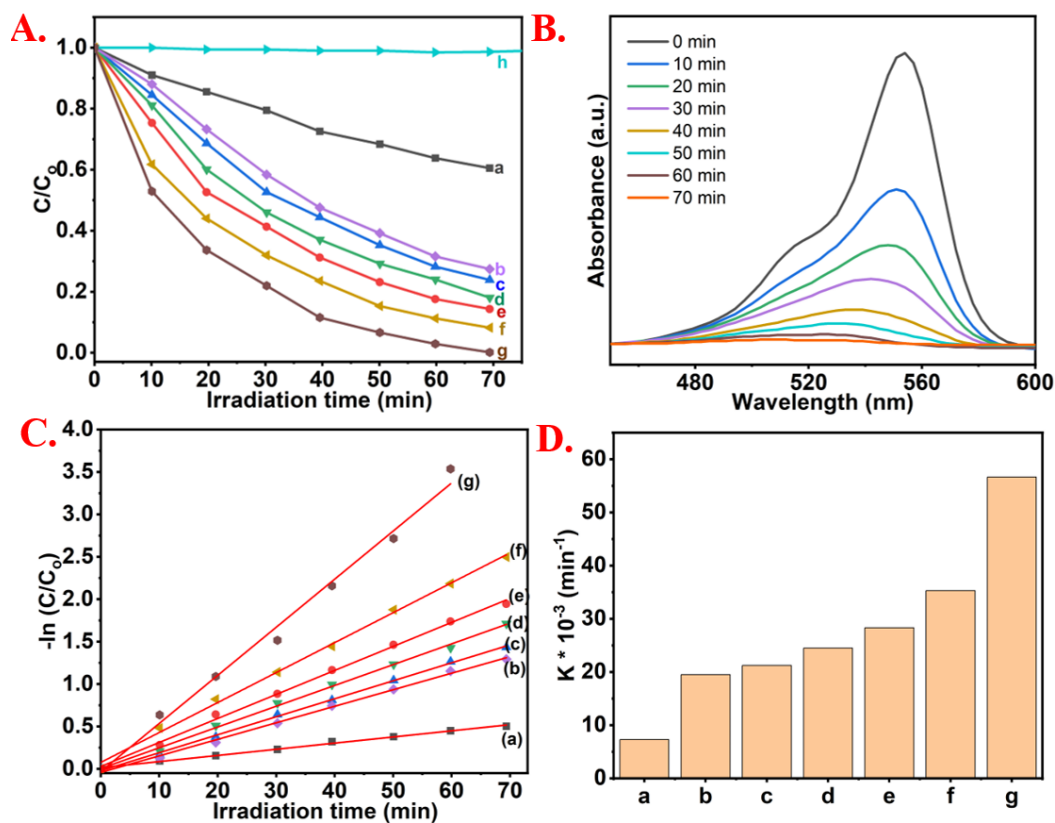
Fig. 6.10 (A) Photocatalyst assisted degradation of Rh B over various composites; 6.10(B). Absorption spectra of Rh B in presence of $Ag_2O/SnO_2@g-C_3N_4$ composite under various sunlight irradiation times; 6.10(C). First-order kinetic plots over various composites and 6.10(D). comparison of rate constant values of (a) $g-C_3N_4$, (b) 25% $SnO_2@g-C_3N_4$, (c) 33% $SnO_2@g-C_3N_4$, (d) 25% $Ag_2O@g-C_3N_4$, (e) 33% $Ag_2O@g-C_3N_4$, (f) 33% $Ag_2O/SnO_2@g-C_3N_4$, and (g) 25% $Ag_2O/SnO_2@g-C_3N_4$-11.

To evaluate the reaction kinetics of dye degradation, $-\ln(C/C_0)$ vs irradiation time was plotted (see Fig. 6.10 C), which fits the first-order reaction. The rate constant (k) for 25% $Ag_2O/SnO_2@g$-C_3N_4-11 was found to be 0.05666 min^{-1} (*cf.* Fig. 6.10 D). This significant improvement in degradation ability was attributed to the optimum ratio of metal oxides viz. 1:1 over the surface of g-C_3N_4 and the synergistic coordination among them. The degradation performance of different ratios of $Ag_2O:SnO_2$ loaded g-C_3N_4 heterostructures was also evaluated as shown in Figure 6.11, the catalytic activity of these different ratios over the g-C_3N_4 structure is a little less for the same loading of metal oxides nanoparticles. A higher ratio of Ag_2O into ternary heterostructure (viz. 4:1 and 2:1) yields a better result, since the presence of Ag_2O over g-C_3N_4 exhibits more separation of charge carriers in PL measurement as seen in fig 6.4(C).

Sunlight provides a large spectrum range which was effectively harnessed by the combination of metal oxides and g-C_3N_4 catalyst, resulting in 100 % degradation of azo dye. 33% $Ag_2O/SnO_2@g$-C_3N_4-11 also exhibits enhanced ability for degradation compared to other binaries.

Other catalysts follow the following order:

g-C_3N_4 < 25%$SnO_2@g$-C_3N_4 < 33% $SnO_2@g$-C3N4 < 25%$Ag_2O@g$-C_3N_4 < 33%$Ag_2O@g$-C_3N_4

The photodegradation process proceeds through adsorption of dye species over the surface of the photocatalyst, however greater surface area of photocatalyst does not always result into greater degradation activity as seen in the case of $SnO_2@g$-C_3N_4. Binary $SnO_2@g$-C_3N_4 has a higher specific surface area to $Ag_2O@g$-C_3N_4 (as seen in the surface area analysis section), however, $Ag_2O@g$-C_3N_4 has greater absorption of wavelength and better band gap tuning with g-C_3N_4 (resulting in enhanced separation
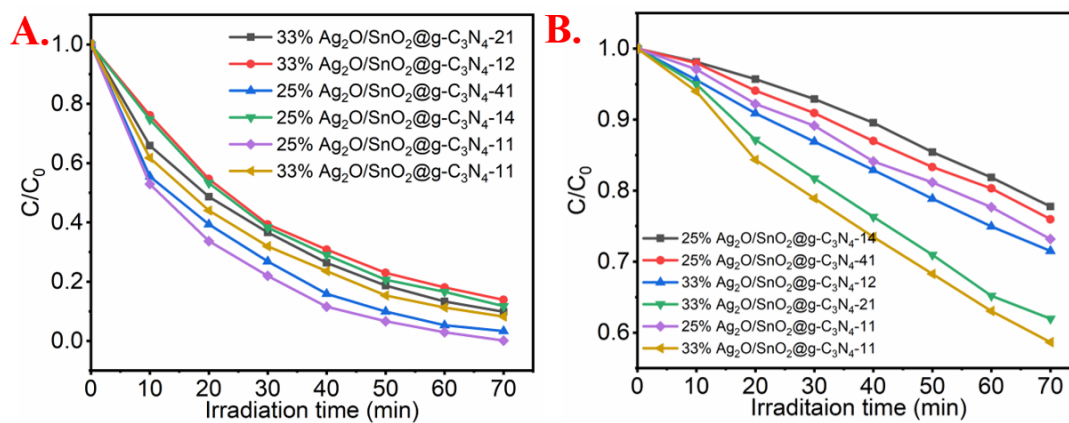
Fig. 6.11 Photocatalytic dye degradation under (A) sunlight exposure and (B) white LED light by different ratios of metal oxide loaded g-C$_3$N$_4$.
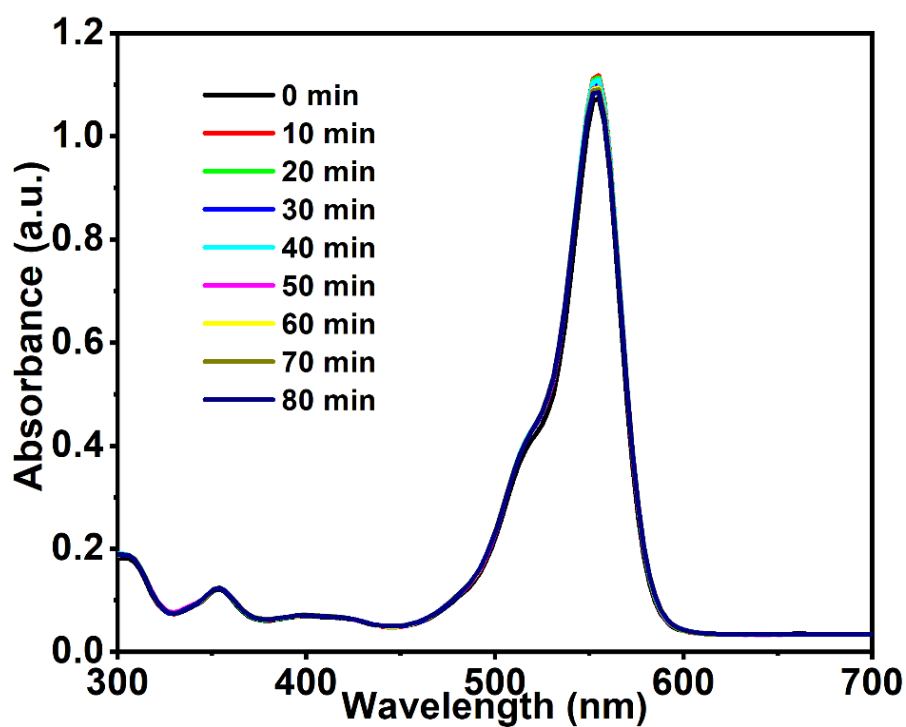

Fig. 6.12 Rh B dye solution irradiation under sunlight in absence of photocatalyst.

of charge carriers) which culminates into higher degradation activity by $Ag_2O@g\text{-}C_3N_4$ among binary counterparts. A test run was also performed in absence of any catalyst, no significant change in dye concentration was observed as shown in Figure 6.12.

Sunlight is a natural light source and catalytic degradation under it is the highly cost-effective strategy for large-scale effluents, although the availability of sunlight is non-uniform and variable in different parts of the world. Another light source chosen for the azo dye photodegradation study was 40 watts white light LED (λ= 450-475 nm) under a closed chamber in the ambient lab environment, where the distance between the light source and dye solution was kept 15 cm with the vertical falling of photons over the dye solution (*see* Fig. 6.13).

Figure 6.13 (A) exhibits the degradation ability of various catalysts in the C/C_0 vs irradiation time plot along with the individual absorbance vs time plot of 33% $Ag_2O/SnO_2@g\text{-}C_3N_4\text{-}11$ (*see* Fig. 6.13 B). 33% $Ag_2O/SnO_2@g\text{-}C_3N_4\text{-}11$ shows 52 % dye degradation ability in the time period of 100 minutes, which is the highest efficiency to any other nanocomposites and $g\text{-}C_3N_4$ alone. The first-order reaction kinetics with a rate constant of 0.00754 min^{-1} was calculated for 33% $Ag_2O/SnO_2@g\text{-}C_3N_4\text{-}11$ from slope value of -ln(C/Co) vs irradiation time plot as shown in Figure 6.13(C). The degradation ability of other ratios of metal oxides loaded ternary nanocomposites follow a similar trend with superiority of 1:1 combination over others for 33% of metal oxide loading (*see* Fig. 6.11 B).
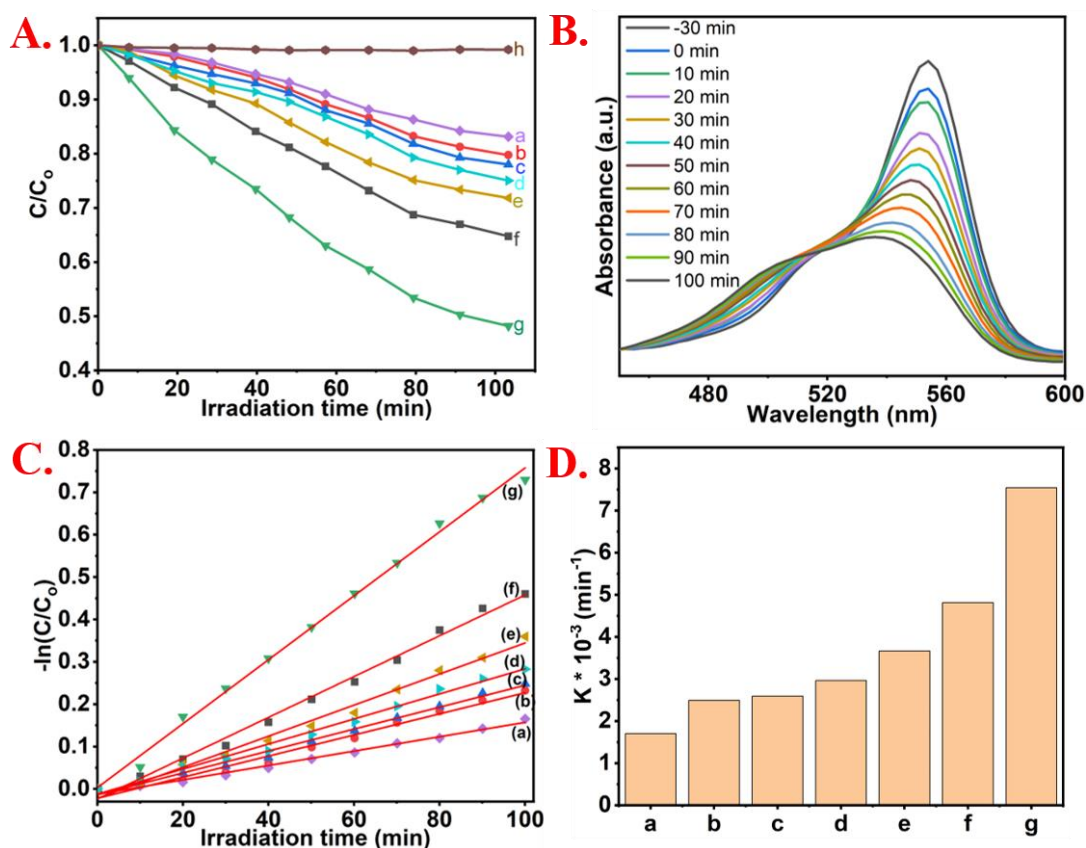
Fig. 6.13 (A) Photocatalyst assisted degradation of Rh B over various composites under white light LED irradiation; 6.13(B) Absorption spectra of Rh B in presence of 33% $Ag_2O/SnO_2@g-C_3N_4$ composite; 6.13(C) First-order kinetic plots over various composites and 6.13(D) comparison of rate constant values of (a) $g-C_3N_4$, (b) 25% $SnO_2@g-C_3N_4$, (c) 25% $Ag_2O@g-C_3N_4$, (d) 33% $SnO_2@g-C_3N_4$, (e) 33% $Ag_2O@g-C_3N_4$, (f) 25% $Ag_2O/SnO_2@g-C_3N_4-11$, and (g) 33% $Ag_2O/SnO_2@g-C_3N_4-11$.

Table 6.3 Rate constants of various catalysts dispersed in dye solution under irradiation from Sunlight and White light LED.

Nanocomposites	Rate constants (x 10^3 min^{-1})	
	Under Sunlight irradiation	Under white light (LED) irradiation
g-C$_3$N$_4$	7.26	1.96
33% Ag$_2$O@g-C$_3$N$_4$	28.30	3.48
33% SnO$_2$@g-C$_3$N$_4$	21.19	2.87
25% Ag$_2$O@g-C$_3$N$_4$	24.49	2.54
25% SnO$_2$@g-C$_3$N$_4$	19.48	2.38
33% Ag$_2$O/SnO$_2$@g-C$_3$N$_4$-11	35.29	7.54
33% Ag$_2$O/SnO$_2$@g-C$_3$N$_4$-12	24.02	4.80
33% Ag$_2$O/SnO$_2$@g-C$_3$N$_4$-21	32.62	7.04
25% Ag$_2$O/SnO$_2$@g-C$_3$N$_4$-11	56.66	4.44
25% Ag$_2$O/SnO$_2$@g-C$_3$N$_4$-14	30.51	3.62
25% Ag$_2$O/SnO$_2$@g-C$_3$N$_4$-41	47.90	3.96

Rate constant values for all the photocatalysts under sunlight and white LED light irradiation are tabulated in Table 6.3 for sake of comparison. As visible from rate constants values of the catalyst under irradiation from two light sources, all the catalysts exhibit 10 times or faster degradation activity when exposed to sunlight. The reduction in degradation ability of ternary catalyst under LED in comparison to sunlight can be correlated to wavelength coverage of light source. Since white light LED has a visible

range of wavelength coverage only, only a limited number of photon interactions will lead to the generation of a limited photogenerated charge carrier and lesser reduction of dye in a given time slot. Sunlight covers a broader spectrum of wavelength, photon from both UV and visible range leads to the generation of charge carriers in the composite material. We also found that there are different optimum ratios of both metal oxides over the g-C_3N_4 material that excels to other catalysts under different light irradiation, as 25% Ag_2O/SnO_2@g-C_3N_4 combination excels under sunlight, while 33% Ag_2O/SnO_2@g-C_3N_4 outperform others under white LED light. The different performance under different light sources is attributed to the combination of factors viz. available wavelength, different mass loading, surface area and optimum ratios of semiconductors. A comparison of C/Co *vs* irradiation time plot of best catalysts under both light sources is given in Figure 6.14 along with a rate constant plot to get a quantitative estimation of degradation efficiency.
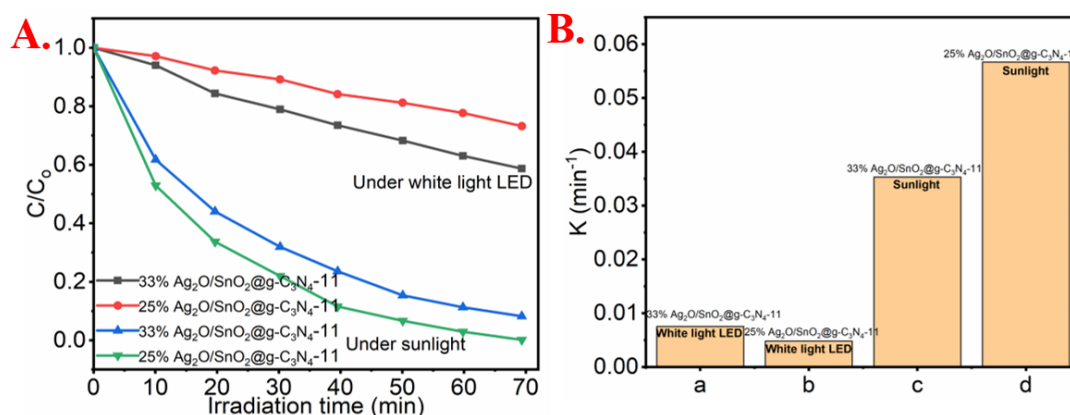
Fig. 6.14(A) Comparison of dye degradation efficiency under two different light sources and 6.14(B) their corresponding rate constant plot; (a and c denotes 33 % Ag_2O/SnO_2@g-C_3N_4-11; b and d denotes 25 % Ag_2O/SnO_2@g-C_3N_4-11)

6.3.6 Scavenger Test (Detection of Active Species) and Stability of the Ternary Nanocomposite

In the degradation process of an organic azo dye, there are active species viz. $^{\bullet}O_2^-$ (superoxide radicals) and $^{\bullet}OH$ (hydroxyl radicals) beside photogenerated charge carriers (e^- and h^+). These active species ($^{\bullet}O_2^-$; $^{\bullet}OH$; e^- and h^+) were detected by the addition of radical scavengers in the dye solution during the degradation study (see Fig. 6.15 A). p-benzoquinone is $^{\bullet}O_2^-$ scavenger, EDTA is h^+ scavenger, dimethyl sulfoxide (DMSO) is e^- scavenger, while methanol quenches $^{\bullet}OH$. The addition of 1 mM p-benzoquinone and EDTA into dye solution cause significant retardation of degradation process with 28% and 35 % reported efficiency respectively for 25% $Ag_2O/SnO_2@g-C_3N_4$ catalyst. Similarly, 50 % and 61 % degradation efficiency were reported respectively in the presence of 1 mM of DMSO and methanol scavengers.
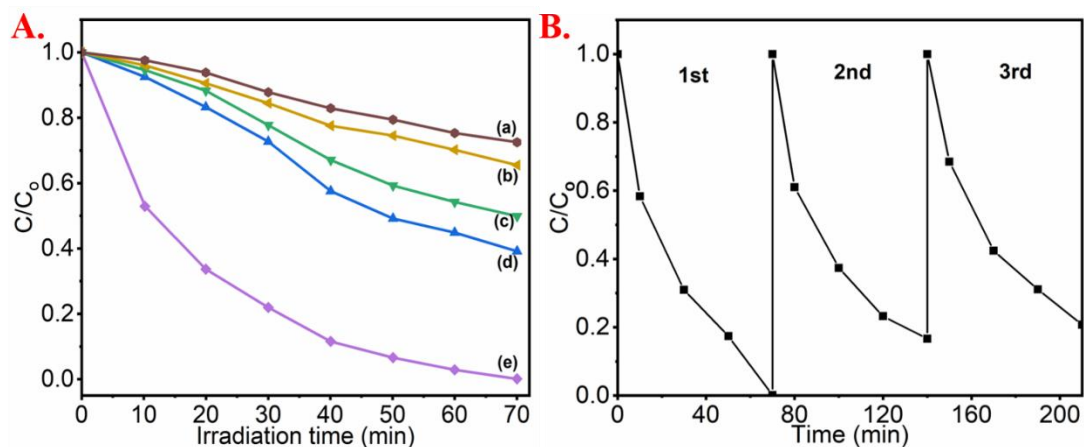

Fig. 6.15(A) Rh B dye degradation in presence of (a) p-benzoquinone, (b) EDTA, (c) DMSO (c) methanol and (e) no scavengers; 6.15(B) reuse-recycle 2nd and 3rd run of 25% $Ag_2O/SnO_2@g-C_3N_4$ composite.

The observed decrease in degradation efficiency verifies the role of active species in the degradation process.

Reusability (recycling) of the catalyst is another important criterion before its large-scale employment. As seen from Figure 6.15(B), we reported ~80 % catalytic activity after the 3rd run for 25% Ag$_2$O/SnO$_2$@g-C$_3$N$_4$ and XRD data confirmed no significant change in the chemical state of the material after repeated use (see Appendix A Fig. A.11). We also carried out the ICP-MS (Inductively coupled plasma-mass spectrometry) analysis of the dye solution to check any possible leaching out of the Ag/Sn traces during the degradation process in the dye solution. The obtained result dictates the no amount of metal traces present in the collected dye solution after the complete degradation process, it establishes the physical stability of the photocatalyst. On the other hand, we also evaluated the total organic carbon (TOC) assay in order to check the mineralization efficiency in the degraded dye solution and obtained TOC removal trend is shown in Figure 6.16(A). In general interpretation, it has been observed that it is hard to achieve high mineralization under exposure of visible radiation, though almost complete degradation of azo dyes. In the present case of study, the mineralization rate is relatively higher under exposure of sunlight compared to white light LED due to the available wide range of radiations responsible for enhanced degradation including mineralization.
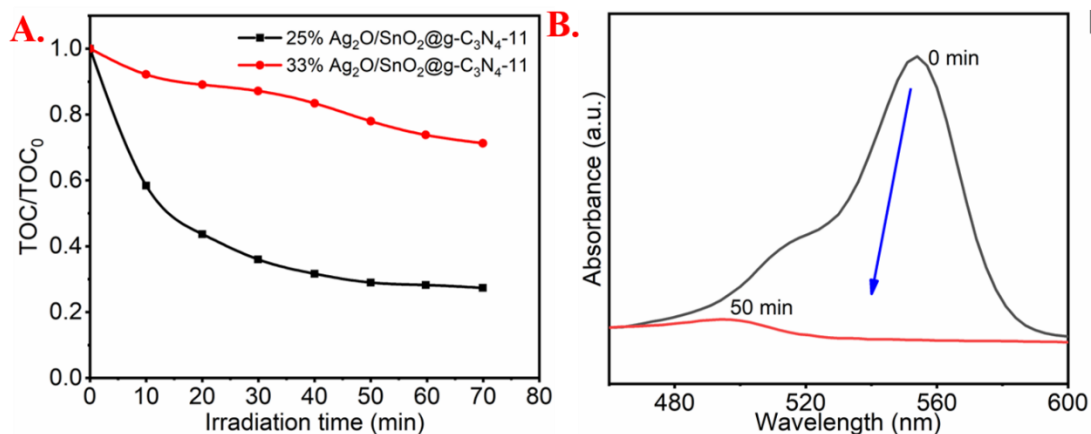
Fig. 6.16(A) TOC evaluation and mineralization efficiency under sunlight and LED for 25% $Ag_2O/SnO_2@g-C_3N_4$ and 33% $Ag_2O/SnO_2@g-C_3N_4$ respectively and (B) UV-vis absorption spectra of industrial effluent before the exposure to the sunlight and after complete degradation of dye using 25% $Ag_2O/SnO_2@g-C_3N_4$-11.

### 6.3.7 Degradation Study of Real Samples Discharged in Industrial Effluent

To study the effectiveness of nanocomposites for real samples, we collected the effluent from a nearby local Handloom factory, where such azo dyes are employed for dying the clothes along with the mixture of binder and thinner. The collected effluent was first filtered using Whatman Filter paper to remove any sediments present. We took the 50 ml of filtered effluent and loaded the 50 mg of Nano-catalyst 25% $Ag_2O/SnO_2@g-C_3N_4$ for degradation study. Figure 6.16(B) shows the UV-vis absorption spectra of effluent just before the exposure to sunlight and after the complete disappearance of the color of effluent. It takes 50 minutes for complete suppression of Rh B (characteristics peak at 450 nm) present in industrial effluent. The real sample

analysis verifies the supremacy of ternary composites as cost-effective pollutant remediators using a natural light source.
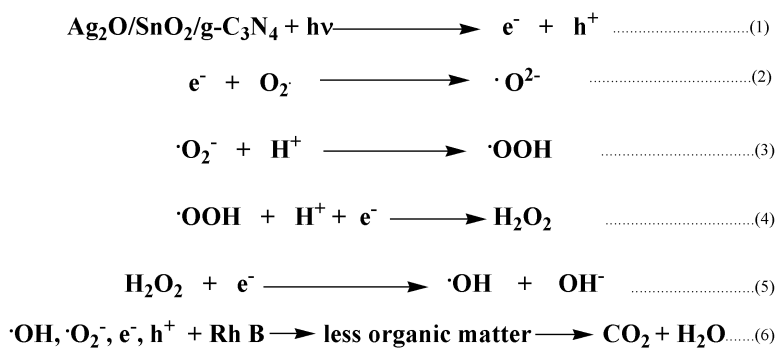
6.3.8 Mechanism of Dye Degradation

Figure 6.17 represents the transfer pathway of photogenerated charge carriers that culminates into dye degradation by the ternary catalyst. Upon irradiation of the catalyst dispersed in the dye solution, photon (hν) interaction leads to the generation of charge carriers, e^- in the conduction band and an equal amount of h^+ in the valence band (as per Eq. 1). The E_{CB} = -1.3 eV (*vs* SHE) of g-C_3N_4 being lower to potential required for $O_2 \rightarrow {}^\bullet O_2^-$ i.e., +0.13 (*vs* SHE) could produce superoxide radicals from dissolved oxygen. A similar case exists for SnO_2 with E_{CB} = -0.1 (*vs* SHE), but in the case of Ag_2O, E_{CB} is +0.2 eV (*vs* SHE), being higher to potential required for $O_2 \rightarrow {}^\bullet O_2^-$, it cannot convert dissolved oxygen into superoxide radicals alone but it assists synergistically when present along with prepared composite $SnO_2@$g-C_3N_4. The conduction band of g-C_3N_4 being above both Ag_2O and SnO_2, photogenerated e^- is transferred to CB of Ag_2O and SnO_2 both acting as electron pool, from here electrons are trapped by dissolved oxygen (O_2) producing dye degrading active species ${}^\bullet O_2^-$. The superoxide radical (${}^\bullet O_2^-$) further reacts with H_2O to give another active species hydroxyl radical (${}^\bullet OH$) through a series of intermediate reactions (Eq. 3-5).

Another photogenerated charge carrier h^+ remains present at the valence band of composites. Since the standard redox potential required for $H_2O \rightarrow {}^\bullet OH$ conversion is 2.68 eV (*vs* SHE) and E_{VB} of Ag_2O and g-C_3N_4 (+1.5 eV and +1.4 eV *vs* SHE respectively) are lower to $E_{{}^\bullet OH/H2O}$, h^+ present on these VB could not oxidize H_2O to
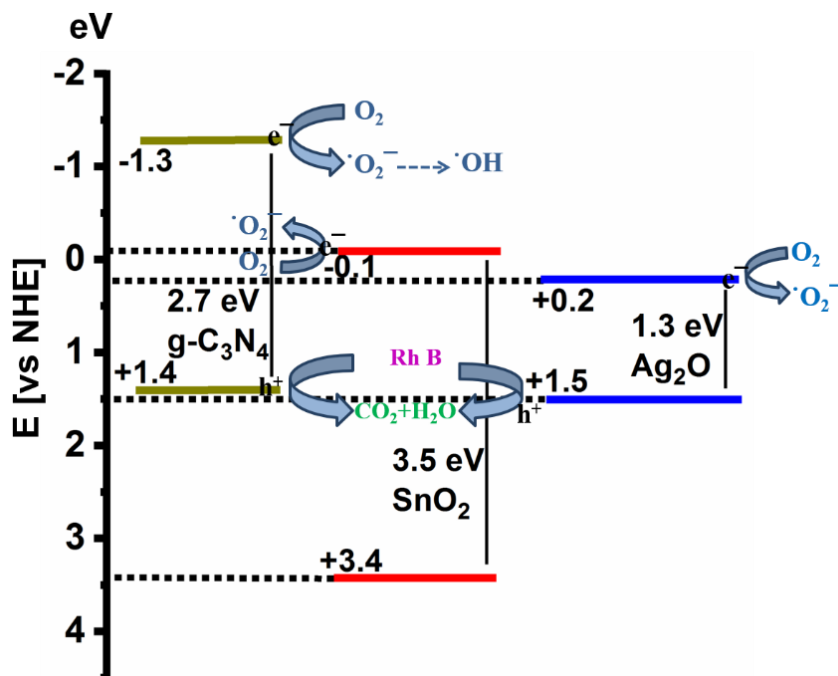
Fig. 6.17 Proposed plausible dye degradation mechanism over the prepared catalyst.

$^{\bullet}$OH, instead of reacts directly with Rh B. Any h^+ present on VB of SnO_2 ($E_{VB} = +3.4$ eV) may take part in $H_2O \rightarrow {}^{\bullet}OH$ conversion by virtue of higher E_{VB} of SnO_2 to $E_{{}^{\bullet}OH/H2O}$. In this way, through the optimum combination of Ag_2O and SnO_2 in the $g\text{-}C_3N_4$ composites, recombination of photogenerated e^- and h^+ in the composite is inhibited to an extent by in-between energy barriers. The reactive species ($^{\bullet}O_2^-$ and $^{\bullet}OH$) generated in the whole process including e^- and h^+ oxidize and degrade Rh B effectively into lesser harmful organic products and ultimately into CO_2 and H_2O (Eq. 6).

$$Ag_2O/SnO_2/g\text{-}C_3N_4 + h\nu \longrightarrow e^- + h^+ \quad \text{.......................(1)}$$

$$e^- + O_2 \longrightarrow \cdot O^{2-} \quad \text{.......................(2)}$$

$$\cdot O_2^- + H^+ \longrightarrow \cdot OOH \quad \text{.......................(3)}$$

$$\cdot OOH + H^+ + e^- \longrightarrow H_2O_2 \quad \text{.......................(4)}$$

$$H_2O_2 + e^- \longrightarrow \cdot OH + OH^- \quad \text{.......................(5)}$$

$$\cdot OH, \cdot O_2^-, e^-, h^+ + Rh\ B \longrightarrow \text{less organic matter} \longrightarrow CO_2 + H_2O \text{.......(6)}$$

Earlier research on photocatalytic degradation of dye has used artificial light sources of high-power Xenon lamp (300/500 Watt) with UV and IR filters to narrow down the spectrum range of emitted light. In our case, we achieved ~100 % dye degradation under natural sunlight using the whole spectrum range available from sunlight for 25% $Ag_2O/SnO_2@g\text{-}C_3N_4$, it greatly reduces degradation costs and puts it for large-scale application purposes.   For experiments in ambient lab conditions, we used commercially available single white light LED (40 watts), greatly reducing the dependence on the sophisticated light source and achieved ~ 52 % of dye degradation by 33 % $Ag_2O/SnO_2@g\text{-}C_3N_4$ in the time period of 100 minutes. Hence, our whole photocatalytic dye degradation set-up was quite cheap economically in comparison to previous reports. Unlike of multistep synthesis approach in some of earlier reports of synthesis of heterostructure catalyst, our synthesis method is simple involving precipitation and hydrothermal techniques for metal oxide nanoparticles synthesis and their decoration over the g-C_3N_4. [252] A table comprising earlier up-to-date reports of g-C_3N_4 based photocatalyst for photodegradation is provided in Table 6.4, the obtained rate constant for our photocatalyst is higher to most of the reported works.

Table 6.4 Comparison of the photocatalytic performance of the as-proposed

nanocomposite with earlier research works.

Photo-Catalyst	Dye	Light Source	Irradiation Time (min)	Degradation %	Rate Constant	Ref.
PANI–g-C_3N_4 composite (0.5:10)	Methylene Blue	500 W Xe lamp	120	92.8	0.02082 min^{-1}	228
PVC:g-C_3N_4 (1:300)	Rh B	300 W iodine tungsten lamp	120	98.0	0.0277 mg L^{-1} min^{-1}	229
CN-PDPB (50:2)	Rh B	300 W Xe lamp	60	99.9	-	251
g-CN-NS/Black-TiO_2	Rh B	50 W LED	30	58.2	0.134 min^{-1}	236
SnO_2−ZnO/g-C_3N_4	Rh B	300 W Xe lamp	60	99.9	0.0184 min^{-1}	84
SnO_2@g-C_3N_4 core-shell	Methyl Orange	500 W Xe lamp	120	>80.0	0.013 min^{-1}	238
Ag_2CO_3/ g-C_3N_4-MN-30	Rh B	300 W Xe lamp	30	>90.0	-	239
50 wt% Ag/AgCl/g-C_3N_4	Methylene Blue	300 W Xe lamp	50	100.0	0.078 min^{-1}	240
50 % Ag_3PO_4/ GO/g-C_3N_4	Rh B	300 W Xe lamp	50	94.8%	-	241
1.0 wt% Ag/g-C_3N_4	methyl orange	500 W Xe lamp	180	100%	2.3476 h^{-1}	242
Ag_2O–g-C_3N_4	Rh B	300 W Xe lamp	50	100 %	0.1053 min^{-1}	232
SnO_2/g-CN-72.12%	methyl orange	500 W Xe lamp	100	98.7 %	3.026 min^{-1}	234
TiO_2/Ag_3PO_4/g-C_3N_4	Metronidazole (antibiotic)	24 W LED	80	95.6 %	0.0472 min^{-1}	252
25 % Ag_2O/SnO_2@g-C_3N_4	Rh B	Sunlight	70	99.98 %	0.05666 min^{-1}	Present work

6.4 Conclusions

Different ratios of metal oxides- Ag_2O and SnO_2 decorated g-C_3N_4 nanocomposite was synthesized and implied as an efficient catalytic agent to speed up the Rh B azo dye degradation under irradiation from natural sunlight source and under artificial LED light in ambient lab conditions. The optimal combination of Ag_2O and SnO_2 nanoparticles embedded in the g-C_3N_4 structure exhibit greater absorption of UV-visible spectra and better tuning of bandgap positions, which results in enhanced separation of photogenerated charge carriers. The as-prepared ternary composite 25% $Ag_2O/SnO_2@g$-C_3N_4-11 with 1:1 combination of metal oxides degrades ~100 % Rh B into harmless products in time duration of 70 minutes underexposure of sunlight, while another ternary composite 33% $Ag_2O/SnO_2@g$-C_3N_4-11 degrades ~52 % of Rh B in 100 minutes underexposure of white light LED which are the best time as compared to other ratios of metal oxide loading, binary nanocomposites and even pure g-C_3N_4 alone (7.8 times and 3.5 times rate constant respectively by 25 % and 33 % $Ag_2O/SnO_2@g$-C_3N_4 to pure g-C_3N_4). The different degradation efficiency under different light sources is attributed to varied coverage of wavelength by optimal combination in ternary nanocomposites. The 25% $Ag_2O/SnO_2@g$-C_3N_4-11 exhibits enhanced mineralization under sunlight exposure and 80% catalytic efficiency after 3rd recycle. Our study demonstrates the efficient and cost-effective method for pollutant remediation using g-C_3N_4-metal oxide-based heterostructure.